

Propagation in and scattering from a matched metamaterial having a zero index of refraction

Richard W. Ziolkowski*

*Department of Electrical and Computer Engineering, University of Arizona, 1230 E. Speedway Boulevard,
Tucson, Arizona 85721-0104, USA*

(Received 7 May 2004; published 21 October 2004)

Planar metamaterials that exhibit a zero index of refraction have been realized experimentally by several research groups. Their existence stimulated the present investigation, which details the properties of a passive, dispersive metamaterial that is matched to free space and has an index of refraction equal to zero. Thus, unlike previous zero-index investigations, both the permittivity and permeability are zero here at a specified frequency. One-, two-, and three-dimensional source problems are treated analytically. The one- and two-dimensional source problem results are confirmed numerically with finite difference time domain (FDTD) simulations. The FDTD simulator is also used to treat the corresponding one- and two-dimensional scattering problems. It is shown that in both the source and scattering configurations the electromagnetic fields in a matched zero-index medium take on a static character in space, yet remain dynamic in time, in such a manner that the underlying physics remains associated with propagating fields. Zero phase variation at various points in the zero-index medium is demonstrated once steady-state conditions are obtained. These behaviors are used to illustrate why a zero-index metamaterial, such as a zero-index electromagnetic band-gap structured medium, significantly narrows the far-field pattern associated with an antenna located within it. They are also used to show how a matched zero-index slab could be used to transform curved wave fronts into planar ones.

DOI: 10.1103/PhysRevE.70.046608

PACS number(s): 41.20.Jb, 03.50.De, 81.05.Zx

I. INTRODUCTION

Planar metamaterial realizations of double negative (DNG) metamaterials, i.e., metamaterials in which the permittivity and permeability are both less than zero, as well as double positive (DPS) metamaterials, i.e., metamaterials in which the permittivity and permeability are both greater than zero, have been reported recently, e.g., [1–7]. Within these studies, there have been several demonstrations, both theoretically and experimentally, of planar metamaterials that exhibit a zero index of refraction within a specified frequency band. In particular, by matching the resonances in a series-parallel lumped element circuit realization of a DNG metamaterial at a specified frequency, the propagation constant as a function of frequency continuously passes through zero (giving a zero index) with a nonzero slope (giving a nonzero group speed) in its transition from a DNG region of its operational behavior to a DPS region [8]. Several applications of these series-parallel metamaterials have been proposed and realized, e.g., phase shifters, couplers, and compact resonators.

Several investigations have also presented volumetric metamaterials that exhibit zero-index medium properties; for instance [9–13]. These zero-index electromagnetic band-gap (EBG) structure studies include working in a passband [9–11] and forcing the effective permittivity only to go to zero to initiate a stop band [12,13]. Introducing a radiating source into a zero-index EBG with an excitation frequency that lies within the EBG's passband, Enoch *et al.* produced an extremely narrow antenna pattern [9–11].

These zero-index metamaterials stimulated the present investigation. The properties of passive metamaterials that are matched to free space and have an index of refraction equal to zero are presented. The Drude medium model that was introduced in [14–16] to study causality and other metamaterial properties is used here to define a medium in which the relative permittivity $\text{Re}[\epsilon(\omega_0)/\epsilon_0]=0$ and the relative permeability $\text{Re}[\mu(\omega_0)/\mu_0]=0$ at a specified frequency $f_0 = \omega_0/(2\pi)$. The same Drude model is used for both the permittivity and permeability so that the impedance in the zero-index medium matches that of free space, i.e., the permittivity $\epsilon(\omega) = \epsilon_0(1 + \chi_{\text{Drude}})$ and the permeability $\mu(\omega) = \mu_0(1 + \chi_{\text{Drude}})$ so that the wave impedance $Z(\omega) = \sqrt{\mu(\omega)/\epsilon(\omega)} = \sqrt{\mu_0/\epsilon_0} = Z_0$. One-, two-, and three-dimensional problems corresponding to source configurations are treated analytically. Numerical simulations with the finite difference time domain (FDTD) method of the one- and two-dimensional source problems confirm these results. The FDTD simulator is also used to treat the corresponding one- and two-dimensional scattering problems. In particular, it will be shown that in both the source and scattering configurations the electromagnetic fields in a matched zero-index medium take on a static character in space, yet remain dynamic in time, in such a manner that the underlying physics remains associated with propagating fields. In the same manner it will be shown that once a steady state is achieved, there is zero phase variation at widely separated points in the zero-index medium. Furthermore, these behaviors are used to illustrate why a zero-index metamaterial, such as the zero-index EBG structured medium in [9–11], significantly narrows the far-field pattern of an antenna that is located within it and how a matched zero-index slab could be used to transform curved wave fronts into planar ones.

*FAX: (520) 621-8076.

Email address: ziolkowski@ece.arizona.edu

II. FIELD STRUCTURE IN A ZERO-INDEX MEDIUM

Consider Maxwell's equations:

$$\begin{aligned}\vec{\nabla} \times \vec{E} &= -\partial_t[\mu_0(\vec{H} + \vec{M})], \\ \vec{\nabla} \times \vec{H} &= \partial_t(\epsilon_0\vec{E} + \vec{P}) + \vec{J}, \\ \vec{\nabla} \cdot (\epsilon_0\vec{E} + \vec{P}) &= \rho, \\ \vec{\nabla} \cdot [\mu_0(\vec{H} + \vec{M})] &= 0,\end{aligned}\quad (1)$$

and their time-harmonic forms

$$\begin{aligned}\vec{\nabla} \times \vec{E}_\omega &= -j\omega\mu\vec{H}_\omega, \\ \vec{\nabla} \times \vec{H}_\omega &= j\omega\epsilon\vec{E}_\omega + \vec{J}_\omega, \\ \vec{\nabla} \cdot (\epsilon\vec{E}_\omega) &= \rho_\omega, \\ \vec{\nabla} \cdot (\mu\vec{H}_\omega) &= 0,\end{aligned}\quad (2)$$

where the $\exp(j\omega t)$ convention is assumed throughout so that, for example, $\vec{E}(\vec{r}, t) = \text{Re}[\vec{E}_\omega(\vec{r})\exp(j\omega t)]$ and $\vec{P}_\omega = \epsilon_0\chi_{Drude}(\omega)\vec{E}_\omega$ giving $\epsilon(\omega) = \epsilon_0[1 + \chi_{Drude}(\omega)]$. Now consider a medium in which $\epsilon(\omega) = 0$ and $\mu(\omega) = 0$. The time-harmonic divergence equations then yield $\rho_\omega = 0$, and the time-harmonic curl equations reduce to

$$\begin{aligned}\vec{\nabla} \times \vec{E}_\omega &= 0, \\ \vec{\nabla} \times \vec{H}_\omega &= \vec{J}_\omega.\end{aligned}\quad (3)$$

Since this means $\vec{\nabla} \cdot \vec{J}_\omega = 0$, then the charge conservation equation $j\omega\rho_\omega + \vec{\nabla} \cdot \vec{J}_\omega = 0$ is also satisfied. Thus the spatial components of the total electromagnetic field behave like a combination of a constant electric field and a magnetostatic magnetic field. Their specific values depend on the source and the zero-index medium configuration.

A. One-dimensional analysis

Consider first a one-dimensional (1D) problem with a time-harmonic electric current sheet source

$$\vec{J}_\omega(\vec{r}) = -H_0\delta(z)\hat{x}\quad (4)$$

that is located at the center of a semi-infinite, matched zero-index slab of thickness $2d$ which is surrounded by free space. The current sheet will generate plane waves that propagate along the z -axis. Equations (2) for the fields outside the slab become

$$\begin{aligned}\partial_z E_x &= -j\omega\mu_0 H_y, \\ \partial_z H_y &= -j\omega\epsilon_0 E_x,\end{aligned}\quad (5)$$

while inside it Eqs. (3) become

$$\partial_z E_x = 0,$$

$$\partial_z H_y = H_0\delta(z).\quad (6)$$

Thus we know that outside the slab the fields must take the form

$$\begin{aligned}\vec{E}_\omega(x, y, z) &= e^{-jk_0(|z|-d)}\frac{Z_0 H_0}{2}\hat{x}, \\ \vec{H}_\omega(x, y, z) &= \text{sgn}(z)e^{-jk_0(|z|-d)}\frac{H_0}{2}\hat{y} \text{ for } |z| \geq d,\end{aligned}\quad (7)$$

where the free space propagation constant (wave number) $k_0 = \omega\sqrt{\epsilon_0}\sqrt{\mu_0}$, while the fields inside the zero-index slab must have the form

$$\begin{aligned}\vec{E}_\omega(x, y, z) &= \frac{Z_0 H_0}{2}\hat{x}, \\ \vec{H}_\omega(x, y, z) &= \frac{H_0}{2}\text{sgn}(z)\hat{y} \text{ for } -d \leq z \leq d.\end{aligned}\quad (8)$$

One finds by inspection that the fields are continuous across the boundaries $z = \pm d$ and that the proper discontinuity of the magnetic field across the source sheet at $z = 0$ is recovered. One also finds that the average power density

$$\langle \vec{S}_\omega \rangle = (1/2)\text{Re}(\vec{E}_\omega \times \vec{H}_\omega^*) = (1/8)Z_0|H_0|^2\text{sgn}(z)\hat{z}\quad (9)$$

is along the $+z$ -axis ($-z$ -axis) for $z > 0$ ($z < 0$) both inside the slab and outside it. Note that one could have defined the solution inside the slab by first assigning to it a plane wave form with the propagation constant $k = \omega\sqrt{\epsilon}\sqrt{\mu}$ rather than with k_0 and then taking the limit $k \rightarrow 0$ to obtain Eq. (9).

If the source is driven with the time history $f(t)$, then the corresponding time domain results within the slab are simply

$$\vec{E}(x, y, z, t) = \frac{Z_0 H_0}{2}f(t)\hat{x},$$

$$\vec{H}(x, y, z, t) = \frac{H_0}{2}\text{sgn}(z)f(t)\hat{y} \text{ for } -d \leq z \leq d\quad (10)$$

and outside it are

$$\vec{E}(x, y, z, t) = \frac{Z_0 H_0}{2}f(t - [|z| - d]/c)\hat{x},$$

$$\vec{H}(x, y, z, t) = \frac{H_0}{2}\text{sgn}(z)f(t - [|z| - d]/c)\hat{y} \text{ for } |z| > d.\quad (11)$$

Thus, one finds that the 1D field structure generated by a time varying source in a matched zero-index slab exhibits a constant spatial distribution within the slab that varies temporally while maintaining the entire propagating plane wave structure outside it.

B. Two-dimensional analysis

In the same manner, consider the two-dimensional (2D) problem of an infinite electric current filament along the z -axis

$$\vec{J}_\omega(\rho, \phi, z) = I_0 \frac{\delta(\rho)}{2\pi\rho} \hat{z} \quad (12)$$

that is embedded in a matched, zero-index semi-infinite cylinder of radius a that is centered along the z -axis. The solutions of Eq. (3) inside the zero-index cylinder for the magnetostatic line source configuration is obtained immediately with Ampère's law. The electric field will again be a constant and should be directed along the electric current direction. Consequently, the fields inside the cylinder have the forms

$$\begin{aligned} \vec{E}_\omega(\rho, \phi, z) &= C_{int} \hat{z}, \\ \vec{H}_\omega(\rho, \phi, z) &= \frac{I_0}{2\pi\rho} \hat{\phi}, \end{aligned} \quad (13)$$

where C_{int} is a constant amplitude. On the other hand, the electromagnetic field generated by a line source in free space is well known [17]. Thus, the fields satisfying Eq. (2) outside the matched zero-index cylinder have the forms

$$\begin{aligned} \vec{E}_\omega(\rho, \phi, z) &= -C_{ext} \frac{\omega\mu_0 I_0}{4} H_0^{(2)}(k_0\rho) \hat{z}, \\ \vec{H}_\omega(\rho, \phi, z) &= -C_{ext} \frac{jk_0 I_0}{4} H_1^{(2)}(k_0\rho) \hat{\phi}, \end{aligned} \quad (14)$$

where $H_n^{(2)}(x)$ is the Hankel function of type 2, order n and the constant C_{ext} has been introduced to allow satisfaction of the boundary conditions at the interface $\rho=a$.

Applying the boundary conditions that the tangential components of the electric and magnetic field must be continuous across the interface at $\rho=a$, one obtains

$$\begin{aligned} \vec{E}_\omega(\rho, \phi, z) &= \begin{cases} -\frac{Z_0 I_0 j H_0^{(2)}(k_0 a)}{2\pi a H_1^{(2)}(k_0 a)} \hat{z} & \text{for } \rho \leq a, \\ -\frac{Z_0 I_0 j H_0^{(2)}(k_0 \rho)}{2\pi a H_1^{(2)}(k_0 a)} \hat{z} & \text{for } \rho > a, \end{cases} \quad (15) \\ \vec{H}_\omega(\rho, \phi, z) &= \begin{cases} \frac{I_0}{2\pi\rho} \hat{\phi} & \text{for } \rho \leq a, \\ \frac{I_0}{2\pi a} \frac{H_1^{(2)}(k_0 \rho)}{H_1^{(2)}(k_0 a)} \hat{\phi} & \text{for } \rho > a. \end{cases} \quad (16) \end{aligned}$$

It is noted that the far-field ratio of the field components properly recovers the wave impedance, i.e., $\lim_{\rho \rightarrow \infty} E_z/H_\phi = -Z_0$. This conclusion follows from the asymptotic result $\lim_{\rho \rightarrow \infty} H_n^{(2)}(\zeta) = j^n \sqrt{2/\pi\zeta} \exp[-j(\zeta - \pi/4)]$ for integer n . Using the Wronskian identity (54:5:6) of [18] one has $J_{n+1}(\zeta)Y_n(\zeta) - J_n(\zeta)Y_{n+1}(\zeta) = 2/(\pi\zeta)$. This means $\text{Re}\{jH_0^{(2)}(\zeta) \times [H_1^{(2)}(\zeta)]^* \} = J_1(\zeta)Y_0(\zeta) - J_0(\zeta)Y_1(\zeta) = 2/(\pi\zeta)$. Consequently, the average Poynting's flux both inside and outside the cylinder can be expressed in the form

$$\langle \vec{S}_\omega \rangle = -(1/2)\text{Re}(E_{\omega,z} H_{\omega,\phi}^*) \hat{\rho} = \frac{Z_0 I_0^2}{(2\pi a)^2} \frac{1}{|H_1^{(2)}(k_0 a)|^2} \frac{2}{\pi k_0 \rho} \hat{\rho}. \quad (17)$$

The power flow is thus pointed in the outward direction in both cases.

The time variation form of the electromagnetic field inside the matched zero-index cylinder is complicated slightly by the presence of the wave number and hence the frequency in the field component terms. Only the magnetic field within the zero-index cylinder is straightforward. In particular, for $\rho < a$,

$$\vec{H}(\rho, \phi, z, t) = \frac{I_0}{2\pi\rho} f(t) \hat{\phi}. \quad (18)$$

The spatial and temporal behaviors of this field are decoupled; its spatial variation exhibits the expected spatial magnetostatic behavior. The electric field component must be obtained by Fourier transform, e.g., taking $F(\omega)$ to be the Fourier transform of $f(t)$ and recognizing that $k_0 = \omega/c$, the time domain electric field within the matched zero-index cylinder is

$$\vec{E}(\rho, \phi, z, t) = -\frac{Z_0 I_0}{2\pi a} \int_{-\infty}^{\infty} e^{j\omega t} F(\omega) \frac{jH_0^{(2)}(\omega a/c)}{H_1^{(2)}(\omega a/c)} \frac{d\omega}{2\pi} \hat{z}, \quad (19)$$

which does not yield a closed form result in general. Nonetheless, if the spectrum is centered mainly at f_0 and $2\pi f_0 a/c$ is large enough for the asymptotic approximation for the Hankel functions to be appropriate, then for $\rho < a$

$$\vec{E}(\rho, \phi, z, t) \approx -\frac{Z_0 I_0}{2\pi a} f(t) \hat{z}. \quad (20)$$

The electric field, being constant spatially, thus varies coherently in time with the magnetic field.

C. Three-dimensional analysis

Finally, consider the corresponding three-dimensional (3D) problem. A time-harmonic, z -oriented infinitesimal dipole with current moment $I_0 \ell$ [the corresponding dipole moment is $p_0 = I_0 \ell / (-j\omega)$] is located at the origin. The current density thus has the form

$$\vec{J}_\omega(\vec{r}) = I_0 \ell \delta(\vec{r}) \hat{z}. \quad (21)$$

The dipole is assumed to be surrounded by a zero-index medium sphere of radius a that is also centered at the origin, and this sphere is surrounded by free space. The magnetic field curl equation in Eq. (3) can be replaced with the vector potential equation

$$\nabla^2 \vec{A}_{\omega,h} = -\vec{J}_\omega, \quad (22)$$

where the modified vector potential $\vec{A}_{\omega,h}$ is related to the magnetic field (rather than to the magnetic induction field) through the relation $\vec{H}_\omega = \vec{\nabla} \times \vec{A}_{\omega,h}$. It has the solution

$$\vec{A}_{\omega,h} = \frac{I_0 \ell}{4\pi r} \hat{z} = \frac{I_0 \ell}{4\pi r} [\hat{r} \cos \theta - \hat{\theta} \sin \theta]. \quad (23)$$

Consequently, in the matched zero-index sphere the magnetic field satisfying Eq. (3) is

$$\vec{H}_\omega = \frac{I_0 \ell}{4\pi r^2} \hat{\phi} \sin \theta \quad (24)$$

and the corresponding electric field in rectangular coordinates is constant:

$$\vec{E}_\omega = C_{int} \hat{z} = C_{int} [\hat{r} \cos \theta - \hat{\theta} \sin \theta]. \quad (25)$$

On the other hand, the fields that satisfy Eq. (2) outside the matched zero-index sphere are proportional to the well-known infinitesimal dipole antenna expressions [19]

$$E_r(\vec{r}, \omega) = C_{ext} \frac{2Z_0 I_0 \ell}{r} \left(1 + \frac{1}{jk_0 r}\right) \frac{e^{-jk_0 r}}{4\pi r} \cos \theta,$$

$$E_\theta(\vec{r}, \omega) = C_{ext} jk_0 Z_0 I_0 \ell \left(1 + \frac{1}{jk_0 r} - \frac{1}{(k_0 r)^2}\right) \frac{e^{-jk_0 r}}{4\pi r} \sin \theta,$$

$$H_\phi(\vec{r}, \omega) = C_{ext} jk_0 I_0 \ell \left(1 + \frac{1}{jk_0 r}\right) \frac{e^{-jk_0 r}}{4\pi r} \sin \theta,$$

$$E_\phi(\vec{r}, \omega) = H_r(\vec{r}, \omega) = H_\theta(\vec{r}, \omega) = 0. \quad (26)$$

Applying the continuity of the tangential field component boundary conditions at the interface $r=a$, one can solve for the unknown coefficients C_{int} and C_{ext} . With the wave impedance of the exterior dipole field at the radius $r=a$ being

$$Z_{dipole} = \frac{E_\theta(r=a, \theta, \phi, \omega)}{H_\phi(r=a, \theta, \phi, \omega)} = \frac{Z_0}{jk_0 a} \frac{1 + jk_0 a - (k_0 a)^2}{1 + jk_0 a} \quad (27)$$

one obtains

$$C_{int} = -\frac{Z_{dipole} I_0 \ell}{4\pi a^2}, \quad (28)$$

$$C_{ext} = \frac{e^{+jk_0 a}}{1 + jk_0 a}. \quad (29)$$

Thus, for clarity, the fields in the matched zero-index sphere have the forms

$$\vec{E}_\omega(r, \theta, \phi) = -\frac{Z_{dipole} I_0 \ell}{4\pi a^2} \hat{z} = -\frac{Z_{dipole} I_0 \ell}{4\pi a^2} [\hat{r} \cos \theta - \hat{\theta} \sin \theta],$$

$$\vec{H}_\omega(r, \theta, \phi) = \frac{I_0 \ell}{4\pi r^2} \hat{\phi} \sin \theta. \quad (30)$$

The electric field is constant; the magnetic field has the expected magnetostatic form spatially. The power flow is orthogonal to the z -axis, i.e., along the $-\hat{z} \times \hat{\phi} = +\hat{\rho}$ direction.

The time domain electric field in the interior of the zero-index sphere is difficult to obtain in general because the impedance Z_{dipole} depends nonlinearly on the frequency. However, if the spectrum is peaked where $k_0 a \gg 1$, then Z_{dipole}

$\approx Z_0$ and the result is straightforward. On the other hand, the time domain magnetic field is readily obtained. Thus, when $Z_{dipole} \approx Z_0$, one has for $r \leq a$

$$\vec{E}(r, \theta, \phi, t) \approx -\frac{Z_0 I_0 \ell}{4\pi a^2} f(t) \hat{z} = -\frac{Z_0 I_0 \ell}{4\pi a^2} f(t) [\hat{r} \cos \theta - \hat{\theta} \sin \theta],$$

$$\vec{H}(r, \theta, \phi, t) = \frac{I_0 \ell}{4\pi r^2} f(t) \hat{\phi} \sin \theta. \quad (31)$$

Thus, the basic spatial field structure in the 3D zero-index medium is again a constant electric field and a magnetostatic magnetic field. These field components are then coherently varying in time. The power flow is real and positively directed away from the current moment axis. The forces experienced in such a zero-index medium are discussed in the Appendix.

III. FDTD SIMULATORS

Both one- and two-dimensional finite difference time domain simulation experiments were conducted. The 1D, 2D, and 3D FDTD simulation environments have been used successfully in a variety of metamaterial studies and has been validated with numerous analytical, numerical, and experimental results. They are described in detail in [14–20]. The one-dimensional simulations considered here used the field and current components E_x , H_y , and J_x . The two-dimensional simulations considered here used the field and current components H_x , H_y , E_z , and J_z .

As in [14–16], lossy Drude polarization and magnetization models were used to simulate the zero-index medium. In the frequency domain, this means the permittivity and permeability were described as

$$\varepsilon(\omega) = \varepsilon_0 \left[1 - \frac{\omega_{pe}^2}{\omega(\omega - j\Gamma_e)}\right], \quad (32)$$

$$\mu(\omega) = \mu_0 \left[1 - \frac{\omega_{pm}^2}{\omega(\omega - j\Gamma_m)}\right]. \quad (33)$$

Several matched zero-index cases were considered. In these cases the parameters for the electric and magnetic Drude models were identical, i.e., $\omega_{pe} = \omega_{pm} = \omega_p$. In all cases, only low loss values were considered by setting $\Gamma = \Gamma_p = \Gamma_m = 1.0 \times 10^{-5} \omega_p$. This means that the index of refraction had the form

$$n(\omega) = \left[\frac{\varepsilon(\omega)\mu(\omega)}{\varepsilon_0\mu_0}\right]^{1/2}$$

$$= 1 - \frac{\omega_p^2}{\omega(\omega - j\Gamma)}$$

$$= 1 - \frac{\omega_p^2}{\omega^2 + \Gamma^2} - j\frac{\Gamma}{\omega} \frac{\omega_p^2}{\omega^2 + \Gamma^2}$$

$$\approx 1 - \frac{\omega_p^2}{\omega^2} - j\frac{\Gamma\omega_p^2}{\omega^3}. \quad (34)$$

Consequently,

$$n_{\text{real}}(\omega) \approx 1 - \frac{\omega_p^2}{\omega^2}. \quad (35)$$

Thus, by adjusting the plasma frequency ω_p , the desired value of n_{real} at a specified frequency was obtained.

In all cases, the center frequency of interest to define the index of refraction was chosen to be $f_0=30$ GHz, corresponding to a free-space wavelength $\lambda_0=1.0$ cm. This value was selected to connect these cases to the one presented in [14–16]. For the zero-index cases, i.e., for $n_{\text{real}}(\omega_0) \approx 0$, these parameters were simply $\omega_p=2\pi f_0=1.885 \times 10^{11}$ rad/s and, hence, $\Gamma=1.885 \times 10^6$ s⁻¹. Note that all of the results to be presented can be achieved in a similar fashion at any desired set of microwave, millimeter, or optical frequencies with the appropriate frequency values in the Drude models and the corresponding FDTD simulation parameters.

The input time signals were all the multiple cycle m - n - m pulses discussed in [14–16]. The function $f(t)$ turns on in m periods, turns off in m periods, and maintains a constant amplitude for n periods. These smooth excitation functions generate minimal noise as the waves are introduced into the FDTD simulation region. All the cases below used continuous wave (cw) signals that were turned on in five-cycles and then were held constant for the entire simulation time T_{total} , i.e., $m=5$ and $(m+n)T_p \gg T_{\text{total}}$. Thus the input time signal had its spectrum centered on f_0 with a very narrow bandwidth.

IV. FDTD RESULTS

The propagation in and scattering from a zero-index metamaterial were simulated in both 1D and 2D configurations to verify the analytical results. The 1D FDTD simulator was used to model the response of an electric current sheet source that was centered in a matched zero-index slab embedded in free space. It was also used to model the scattering of a plane wave from a matched zero-index slab. The 2D FDTD simulator was used to model the response of an electric current filament that is centered in the interiors of infinite circular and rectangular matched zero-index cylinders and that is located exterior to an infinite rectangular matched zero-index cylinder. It was also used to model the scattering of a large waist Gaussian beam from a matched zero-index slab. Those Gaussian beam results, however, are essentially the same as those obtained for the 1D scattering problem; hence, they will not be presented here. In all cases, the predicted zero-index behavior was obtained.

A. 1D FDTD simulations

The 1D problem of an infinite current sheet centered in a matched zero-index medium was simulated first. The spatial discretization, i.e., the cell size, was set at $\Delta z=2.0 \times 10^{-5}$ m= $\lambda_0/500$. The time step Δt was set at 0.95 of the 1D Courant value, i.e., $\Delta t=0.95\Delta z/c=63.333$ fs. The total simulation space was 20 000 cells long; the source was located at the center of this simulation space. The simulation was run for 30 000 time steps. The matched Drude medium slab was 10 200 cells ($20.4\lambda_0$) wide and centered on the

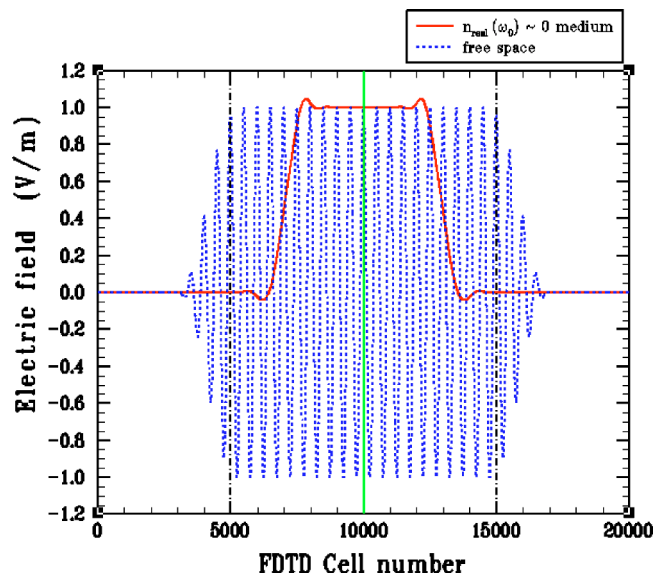


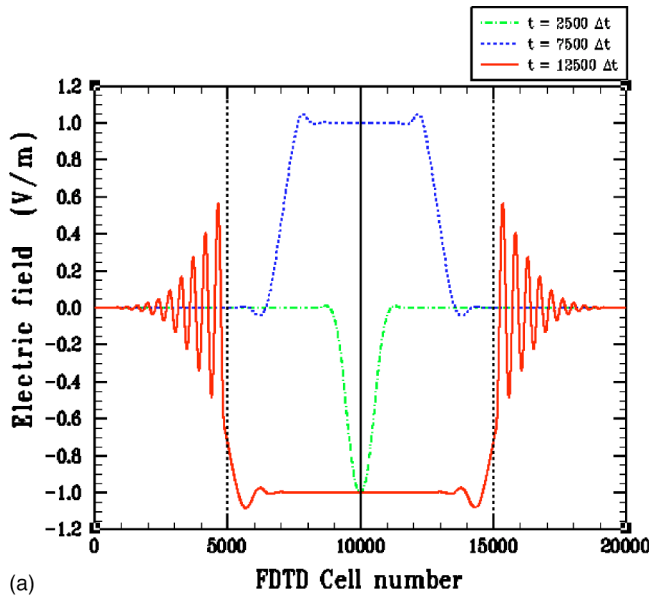
FIG. 1. Comparison of the electric field generated at $t = 7500\Delta t$ by an infinite current sheet driven by a 30 GHz source in a matched zero-index Drude medium slab and in free space.

source; thus the distance from the source to the edge of the slab was $10.2\lambda_0$ in each direction. The noninteger number of wavelengths of this distance was purposely selected to avoid any purely resonant lengths in the depth of the slab. The case of the source radiating in free space was also simulated. The source was an electric current sheet excited with an initial amplitude $H_0/2=1/Z_0$ so that the resulting electric field would have an amplitude of 1.0.

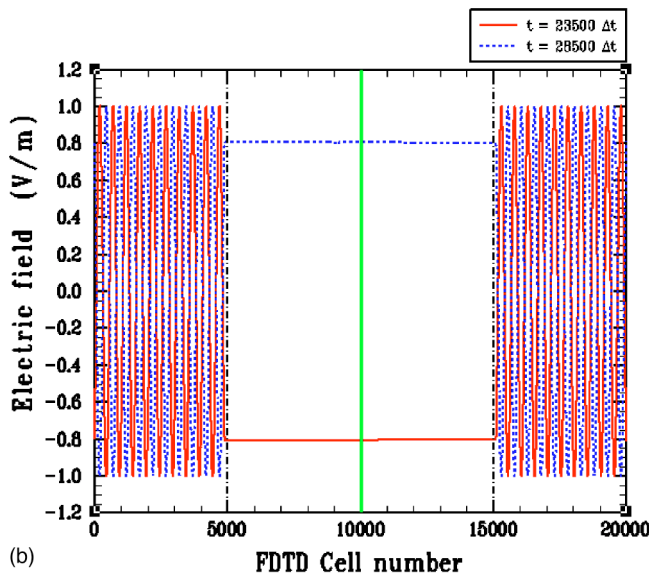
The FDTD predicted electric field values at all points in the simulation space are compared at $t=7500\Delta t$ in Fig. 1 for the matched zero-index slab case (red solid line) and for the corresponding free space case (blue dashed line). The dashed black vertical lines represent the slab boundaries. The solid vertical green line represents the source. The wave fronts are propagating from the source towards both the left and right boundaries of the FDTD simulation region. The free-space result shows that the field quickly reaches its steady-state behavior behind its leading edges. On the other hand, the zero-index result shows the propagation of the envelope of the excitation signal while a constant field amplitude appears to be developing behind these fronts. Close examination of the signal front itself shows that it is actually propagating at the same speed as in the free-space case. Since the signal fronts consist of the highest frequencies in the signal and since the medium looks like free space at those frequencies, this propagation behavior is in agreement with the dispersive behavior discussed in [16]. In contrast, the speed of the envelope itself is approximately $c/2$, i.e., the real part of the propagation constant

$$\beta(\omega) = \frac{\omega}{c} n_{\text{real}}(\omega) = \frac{\omega}{c} \left[1 - \frac{\omega_p^2}{\omega^2 + \Gamma^2} \right] \quad (36)$$

yields the group speed



(a)



(b)

FIG. 2. Electric field generated by the infinite current sheet driven by a 30 GHz source in a matched zero-index Drude medium slab. (a) Early times; (b) late times.

$$v_g(\omega) = (\partial_\omega \beta)^{-1} = \frac{c}{1 + [\omega_p^2(\omega^2 - \Gamma^2)/(\omega^2 + \Gamma^2)^2]} \quad (37)$$

so that at f_0 where $\Gamma/\omega_0 \ll 1$ one has $\beta(\omega_0) \approx 0$ and $v_g(\omega_0) \approx c/2$. This explains the observed (approximately a factor of 2) delay between the signal propagation in free space and in the matched zero-index slab.

A comparison of the electric field distributions in the matched zero-index case for the early times $t=2500\Delta t$, $t=7500\Delta t$, and $t=12500\Delta t$ is given in Fig. 2(a). This confirms the appearance of the constant electric field distribution in the matched zero-index slab. The field has propagated out of the slab by the time $t=12500\Delta t$, and the initial recovery of a free space cw signal propagation behavior outside the

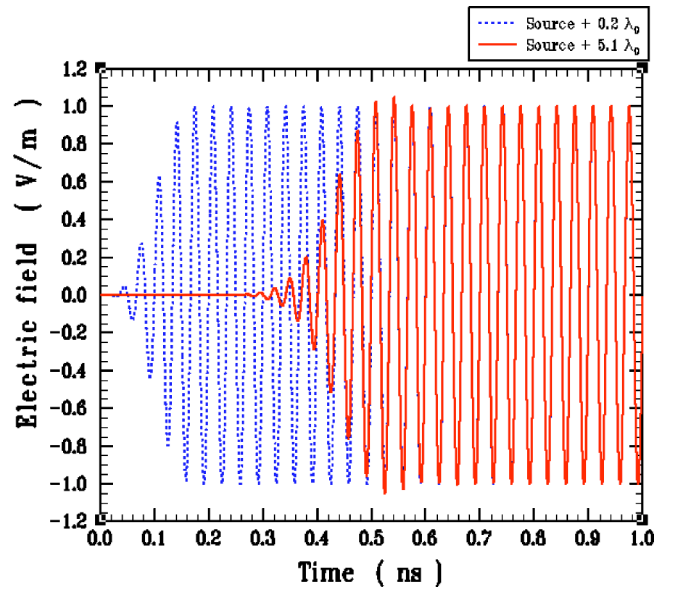


FIG. 3. Comparison of the electric field time histories generated by an infinite current sheet driven by a 30 GHz source in a matched zero-index Drude medium slab at two spatially separated points shows that the phase difference between them is zero.

slab is observed. The late time behavior is shown in Fig. 2(b). The electric field distributions at $t=23500\Delta t$ and at $t=28500\Delta t$ are shown. Inside the matched zero-index slab one observes that the field is spatially constant but varying in time. Outside the slab the field exhibits the free-space cw signal propagation behavior. The field is continuous across the interfaces as shown. Examination of the corresponding magnetic field distributions show that they are scaled versions of the electric field values, the scaling factor being Z_0 . The time histories of the electric field values measured at the points $0.2\lambda_0$ and $5.1\lambda_0$ to the right of the source are shown in Fig. 3. It is immediately observed that there is no phase difference between the two points separated by $4.9\lambda_0$ once a steady state is reached. All of these FDTD results are in complete agreement with the analytical solution given in Sec. II A.

The 1D plane wave scattering from a zero-index slab was simulated next. The spatial and temporal discretization values remained at $\Delta z = 2.0 \times 10^{-5} \text{ m} = \lambda_0/500$ and $\Delta t = 0.95\Delta z/c = 63.333 \text{ fs}$. The total simulation space was 15 000 cells long. A unit amplitude plane wave was initiated in the FDTD simulation region through a total field/scattered field source plane located at $z=1000\Delta z$. The front face of the slab was located at $z=5000\Delta z$, $8\lambda_0$ from the source; and the depth of the slab was $5000\Delta z = 10\lambda_0$.

The FDTD predicted electric field values at all points in the simulation space are compared at $t=13500\Delta t$ for the matched zero-index Drude slab case (red solid curve) and for the corresponding free space case (blue dashed curve) in Fig. 4. The dashed black vertical lines represent the slab boundaries. The incident wave propagates for $8\lambda_0$ before interacting with the slab. The signal propagating in free space has already cleared the slab. In the zero-index slab the leading edge of the envelope of the signal is propagating at approximately half the free space speed. The front edge of the signal

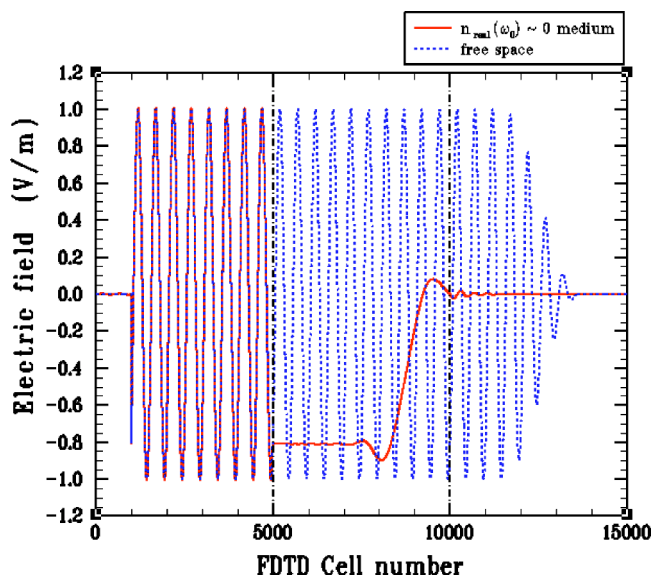


FIG. 4. Comparison at $t=13\,500\Delta t$ of the electric field distribution resulting from a 30 GHz plane wave propagating through a matched zero-index Drude medium slab and propagating in free space.

arrives at the same time as it does in the free-space case. The electric field distributions at the late times $t=24\,000\Delta t$ and $t=30\,000\Delta t$ are shown in Fig. 5. The electric field in the slab is constant spatially, but varying in time, as would be expected from the source problem. The magnetic field in the slab is again Z_0 smaller than the electric field. The fields at the front and back edges of the slab are in lockstep with each other. The time histories for two points in the slab, the first being $4.8\lambda_0$ from the front interface and the second being $0.4\lambda_0$ further into the slab from the first point, are shown in Fig. 6. These two points are separated by 200 cells and are equidistant from the center of the slab. As with the source

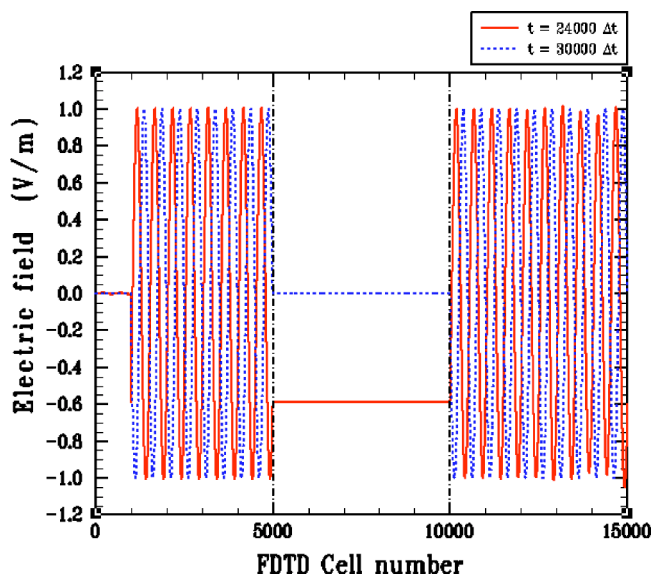


FIG. 5. Electric field distribution at late times resulting from a 30 GHz plane wave propagating through a matched zero-index Drude medium slab.

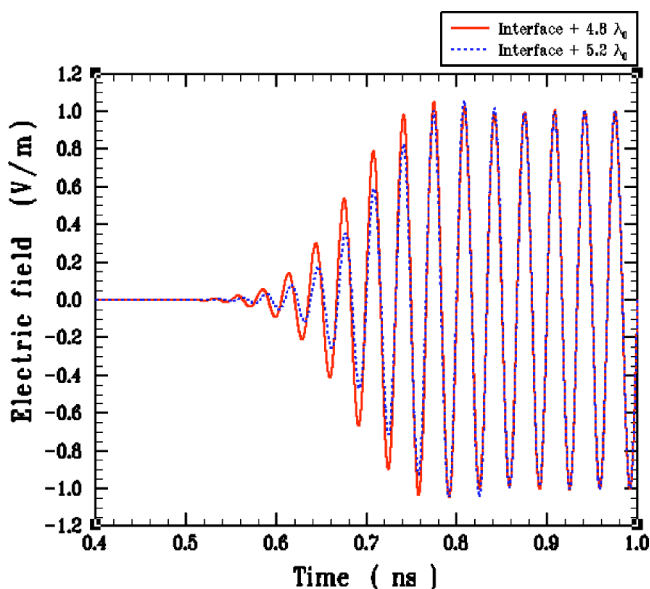


FIG. 6. Comparison of the electric field time histories at two spatially separated points in a matched zero-index Drude medium slab that result from a 30 GHz plane wave propagating through it shows that the phase difference between them is zero.

problem, there is no phase difference between two points in the zero-index slab once steady state has been reached.

B. 2D FDTD simulations

The 2D FDTD environment with a perpendicularly polarized electric field allowed the introduction of an infinite electric line current orthogonal to the simulation space (x versus y , line source along the z -axis). The simulation space was discretized into squares with a side length $\Delta x = \lambda_0/100 = 100\ \mu\text{m}$. The time step was set at 0.95 of the two-dimensional Courant value, i.e., $\Delta t = 0.95\Delta x/(\sqrt{2}c) = 22.39\ \text{ps}$.

The line source was first introduced at the center of a matched zero-index circular cylinder of radius $a = 60\Delta x$. The simulation region was 441 cells \times 441 cells. The line source was located at the center of the cylinder. The driving function was $10^4 f(t)$ to achieve an electric field amplitude on the order of unity in the cylinder. The FDTD generated electric field component E_z and magnetic field component H_x values along the y -axis are shown in Figs. 7(a) and 7(b), respectively, at the late times $t = 1925\Delta t$ and $t = 2000\Delta t$. The electric field distribution in Fig. 7(a) is clearly spatially constant throughout the entire cylinder, but varies in time. On the other hand, one can see in Fig. 7(b) that the magnetic field component within the cylinder has taken on the predicted magnetostatic distribution spatially and also varies in time. Note that along the y -axis the unit vectors $\hat{\phi}(\phi = 90^\circ) = \hat{x}$ and $\hat{\phi}(\phi = 270^\circ) = -\hat{x}$ so that the positive and negative values in Fig. 7(b) yield $H_x \hat{x} \propto (1/\rho)\hat{\phi}$ as predicted by Eq. (18). As shown in Figs. 7(a) and 7(b), the electromagnetic field within the matched zero-index cylinder transitions to an oscillatory, propagating field once it exits the cylinder and enters free space.

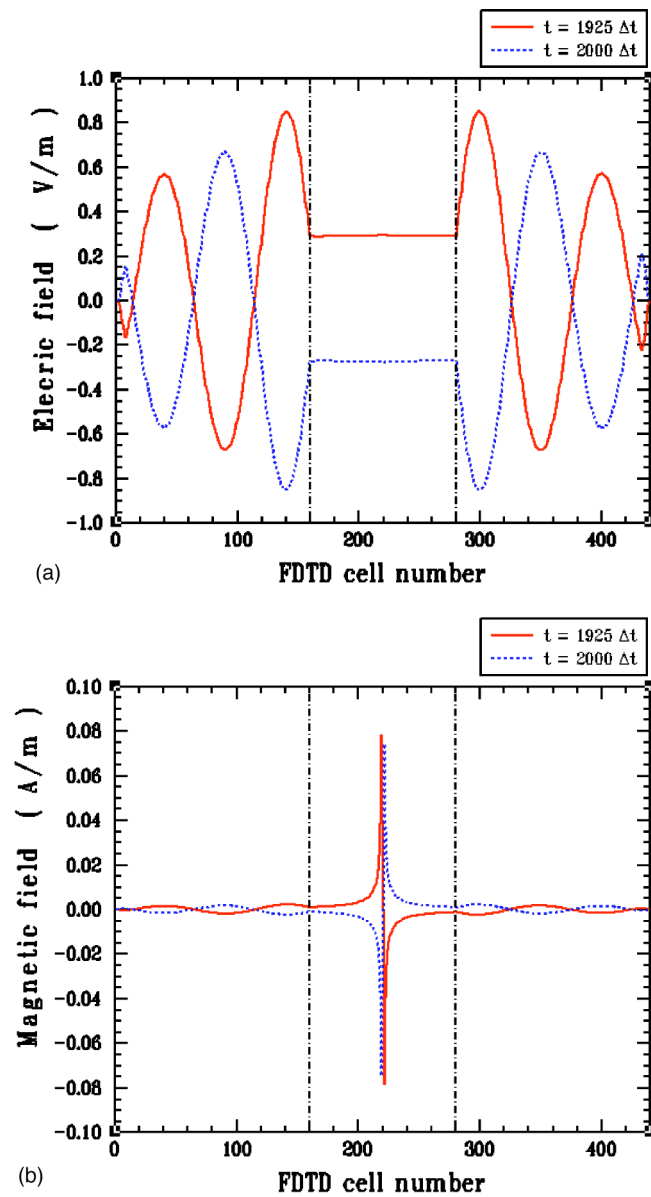


FIG. 7. Field components generated at late times by an infinite line current driven at 30 GHz in a zero-index matched Drude medium cylinder that is surrounded by free space. (a) Electric field E_z ; (b) magnetic field component H_x .

Two-dimensional contour plots of the electric field amplitude are shown in Fig. 8 for the times (a) $t=0$, (b) $t=240\Delta t$, and (c) $t=1800\Delta t$. The x and y axes and the matched zero-index cylinder are shown in Fig. 8(a). The line source is located at the origin at the center of the cylinder. The constant electric field throughout the interior of the cylinder and the propagating field in the exterior region are clearly seen in Fig. 8(c). The sequence shows that the electromagnetic field energy propagates radially outward through the zero-index cylinder into the free-space region. As demonstrated in the 1D case, comparisons of the time histories at various locations within the cylinder show no phase variations between them once steady state has been achieved.

The corresponding electric field amplitude results for the same line source at the center of a square matched zero-index

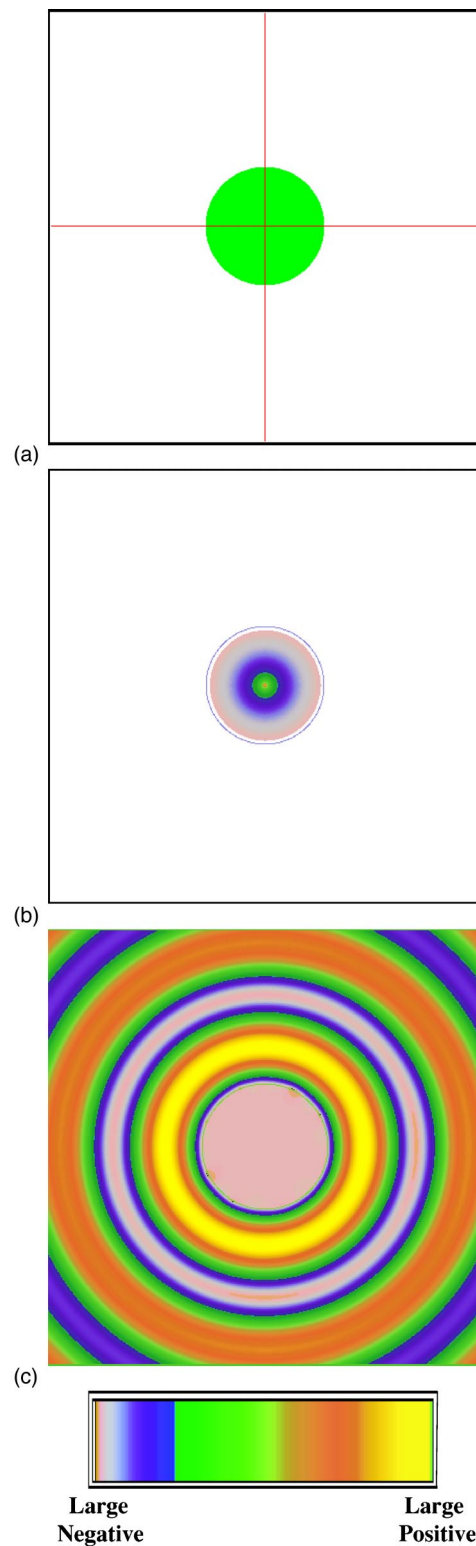


FIG. 8. The electric field distribution produced by an infinite line current driven at 30 GHz and centered in a matched zero-index Drude medium cylinder that is surrounded by free space. (a) $t=0$, (b) $t=240\Delta t$, and (c) $t=1800\Delta t$.

cylinder were also obtained. The square cylinder version allows one to see if corners could cause some issues in the final outcome. It does not. The uniformity of the constant field over the entire interior of the square cylinder was again

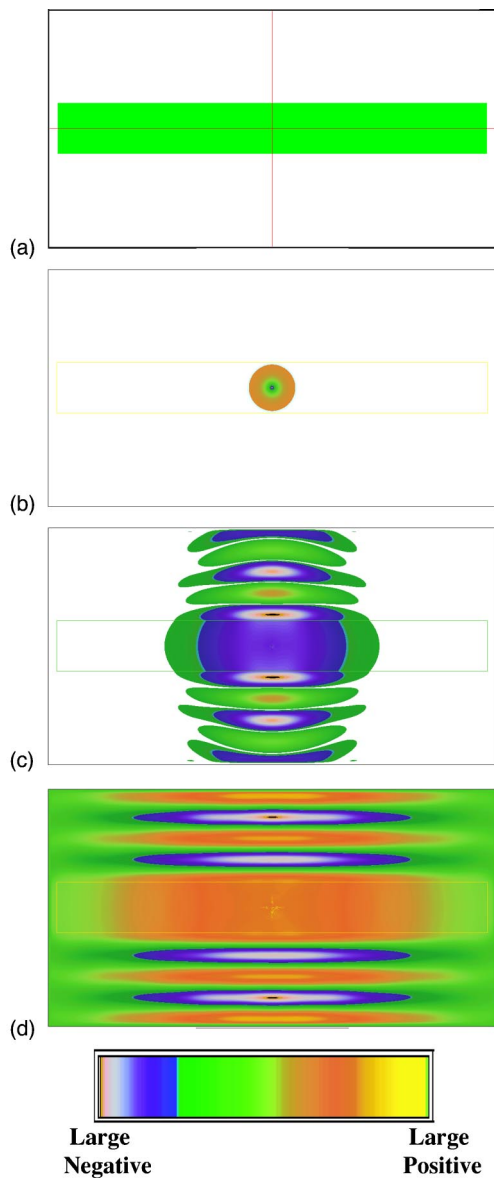


FIG. 9. The electric field distribution produced by a line source driven at 30 GHz and centered in a rectangular matched zero-index Drude medium. (a) $t=0$, (b) $t=200\Delta t$, (c) $t=800\Delta t$, and (d) $t=2200\Delta t$.

obtained. Moreover, one can see that the fields radiated into free space arise locally as though they are driven by uniform fields across apertures corresponding to the sides of the square.

These square cylinder results suggested simulating a geometry corresponding to the directive emission, electromagnetic band-gap structure configurations considered in [9–11]. In particular, the same line source was centered in a 1020 cells \times 120 cells matched zero-index Drude medium slab. The entire FDTD simulation region was 1061 cells \times 561 cells. The electric field amplitude results are shown in Fig. 9 for the times (a) $t=0$, (b) $t=200\Delta t$, (c) $t=800\Delta t$, and (d) $t=2200\Delta t$. The x and y axes and the matched zero-index slab are shown in Fig. 9(a); the source is located at the origin. In Fig. 9(c) one can see that the field radiated from the

zero-index slab propagates away orthogonally to the face of the slab as suggested in [9–11], i.e., from Snell’s law we know that the transmitted waves will have a transmitted angle of zero for any angle of incidence when the index of the incident medium is zero. The cylindrical wave generated by the line source will thus be converted into a wave with a planar wave front as the wave emerges from the matched zero-index slab. Moreover, as the wave propagates from the source outward through the matched zero-index slab, the constant electric field behavior is being established within the slab. This is indeed what is observed in Figs. 9(c) and 9(d). Figure 9(d) also provides an explanation for the highly directive emissions in [9–11]. In steady state, one can see from Fig. 9(d) that the entire face of the slab will have a uniform electric field distribution across it radiating coherently into free space. Figure 9(d) is in agreement with a related frequency domain result given in Fig. 3 of [11]. Because the beam width of the far-field pattern of an aperture is proportional to λ/D , where D is the largest dimension in the aperture, the output beam will become narrower as the aperture is made wider. When a dipole antenna is located in a band-gap structure that acts as a zero-index medium, it is not the source alone nor the local two or three unit cells near the source that characterizes the radiation. Rather, the entire area of the face of the slab determines the far-field radiation behavior. Hence, for a source in the center unit cell of an EBG structure that is, for instance, 20 unit cells wide, the divergence angle of radiation pattern will be approximately 20 times narrower than it would be if only the source were taken into account because the entire structure now plays a role in determining the pattern. In fact, many of the recent reports of highly directional emissions [21–23] from sources modified by EBG or textured surface structures share this same characteristic.

Finally, because the matched zero-index slab transformed the cylindrical waves generated by an internal line source into planar wavefronts, it was anticipated that such a slab would do the same to the fields radiated by an external line source. The slab should create an electromagnetic field within it that has an electric field which is essentially constant spatially throughout, but time varying, when steady-state conditions are attained. This wave front transformer was characterized with the FDTD simulator and the FDTD results confirmed the expected behavior.

The simulation region (x versus y) was 641 cells \times 441 cells. The line source was located along the y -axis. The front of the slab was 100 cells from the line source. The slab dimensions were 600 cells \times 60 cells. The FDTD predicted electric field intensity distributions are shown in Fig. 10 for the times (a) $t=0$, (b) $t=500\Delta t$, (c) $t=1000\Delta t$, and (d) $t=8000\Delta t$. The problem geometry is shown in Fig. 10(a); the source is located at the intersection of the lines in the top half of the figure. The cylindrical fronts from the source have begun interacting with the slab in Fig. 10(b). The initial establishment of the constant electric field in the center of the slab and the start of output waves with flat wave fronts are seen in Fig. 10(c). The essentially spatially constant electric field throughout the slab and output wave fronts parallel to the output face of the slab are seen in Fig. 10(d).

The corresponding electric field amplitude results along the y -axis and along lines parallel to the x -axis are shown in

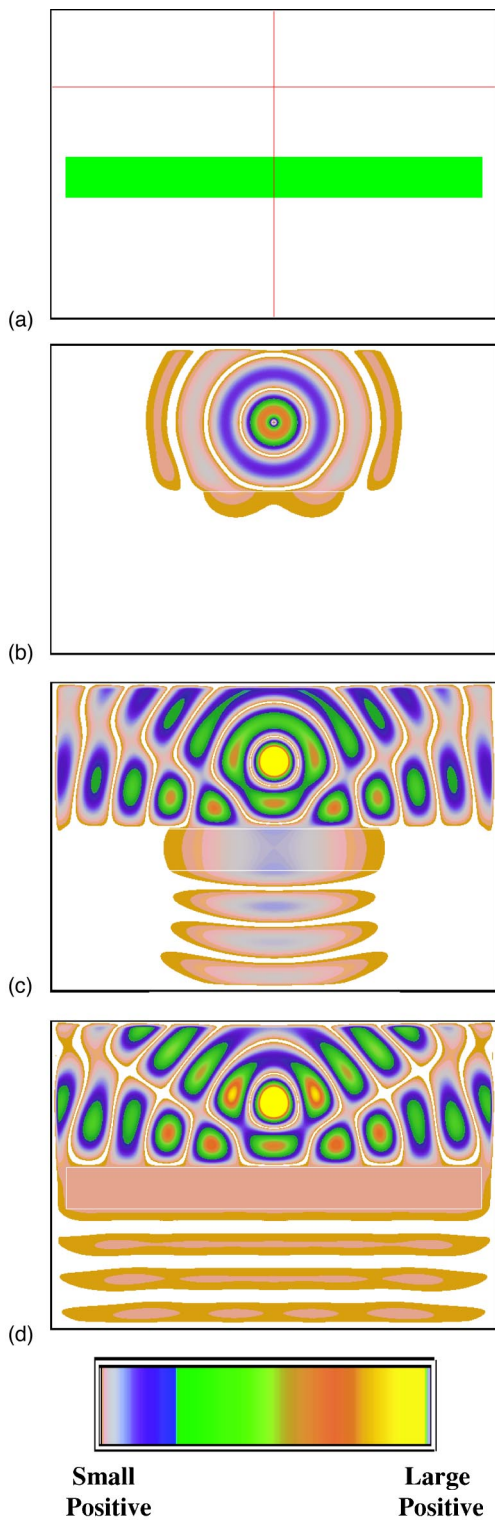


FIG. 10. The electric field intensity distribution produced by a line source driven at 30 GHz external to a rectangular matched zero-index Drude slab. (a) $t=0$, (b) $t=500\Delta t$, (c) $t=1000\Delta t$, and (d) $t=8000\Delta t$.

Figs. 11 and 12, respectively. The results in Fig. 11 are given for $t=5000\Delta t$ and $t=10\,000\Delta t$. The source region dominates the results in Fig. 11(a); the zoom-in results in Fig. 11(b) show that the electric field is spatially constant, but varying

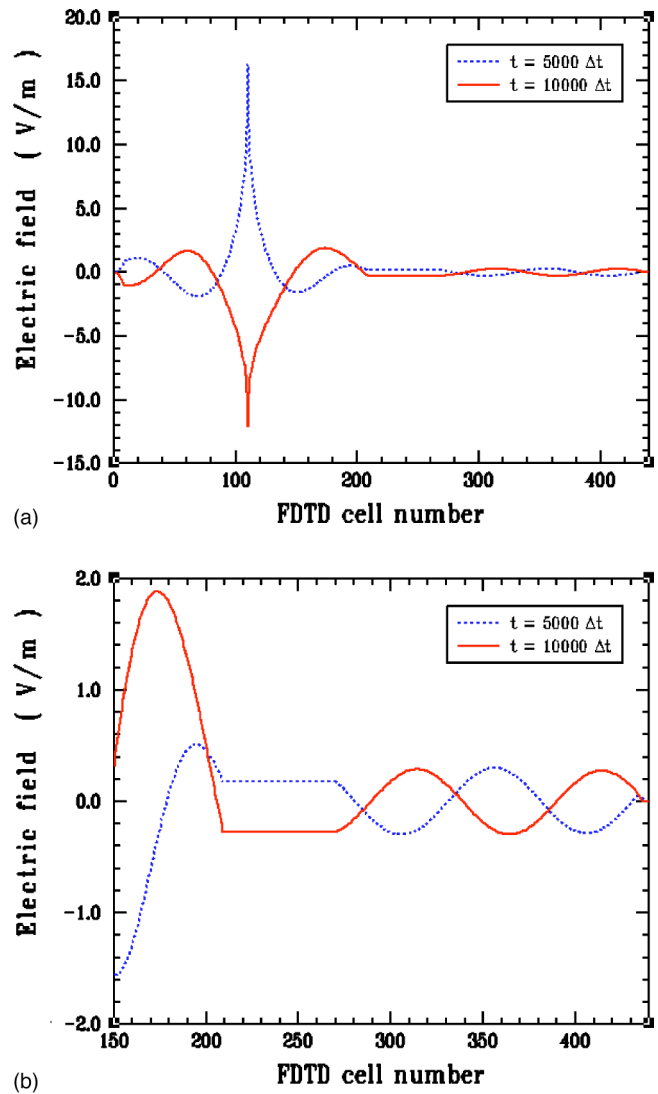


FIG. 11. The FDTD predicted electric field values along the y -axis of the simulation space for an external line source radiating at 30 GHz in the presence of a rectangular matched zero-index Drude medium slab. A spatially constant, time varying electric field intensity is generated within the slab. (a) Electric field along the y -axis; (b) zoom-in.

in time within the slab. The slab is located between cells 210 and 270. The results in Fig. 12 are given for $t=8000\Delta t$ along the line through the center of the slab and at 100 cells from the exit face of the slab. They show that the electric field intensity is nearly constant but with some small ripples across the slab and some larger ripples across the planar wave fronts leaving the slab.

V. CONCLUSIONS

The basic properties of source problems in 1D, 2D, and 3D for a matched zero-index medium were considered analytically. It was demonstrated that in steady state the fields in the matched zero-index medium are static in character but the underlying dynamics are that of propagating transverse

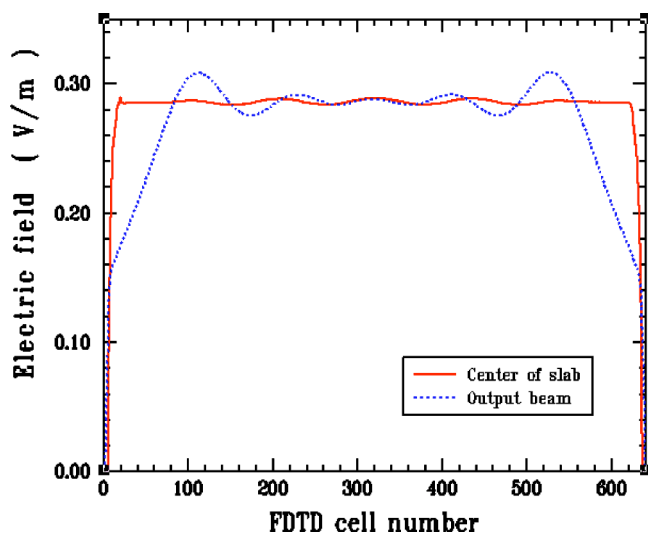


FIG. 12. The FDTD predicted electric field values at $t = 8000\Delta t$ along the transverse centerline of the slab and a transverse line exterior to the slab, 100 cells from the exit face of the slab.

waves. The 1D and 2D predictions were confirmed with FDTD numerical results. A lossy, dispersive Drude medium model was used for all of the FDTD simulations. The corresponding 1D and 2D matched zero-index scattering problems were also investigated with the FDTD simulator. For both the source and scattering problems it was shown that zero phase variation at various points in the matched zero-index medium is achieved once steady-state conditions are obtained. It was also demonstrated that cw sources in matched zero-index media can lead to highly directive beams because the entire medium will eventually radiate coherently in phase.

There may be a variety of potential applications for matched zero-index media beyond their already demonstrated use for compact resonators and highly directive sources. These include delay lines with no phase differences between their inputs and outputs and wave front transformers, i.e., a transformer that converts wave fronts with small curvature into output beams with large curvature (planar) wave fronts. These outcomes were demonstrated successfully with the FDTD simulations of the 1D and 2D scattering problems. The Drude model yielded wave speeds that were $c/2$. Other metamaterials could be designed by engineering the permittivity and permeability models to yield a matched zero-index medium with a tailored wave speed. Complete spatiotemporal wave front engineering could then be realized. Many of these issues are currently being investigated and will be reported in the future.

ACKNOWLEDGMENTS

This work was supported in part by DARPA under Contract No. MDA972-03-100 and by ONR under Contract No. 14-04-1-0320. The author would like to thank Dr. Christophe Caloz and Professor Tatsuo Itoh, UCLA, for interesting discussions concerning planar realizations of zero-index metamaterials and their application to zeroth-order resonators.

APPENDIX

For completeness, let us consider the forces that would exist in a zero-index medium. The mechanical momentum [24,25] reduces in a zero-index medium to the form

$$\vec{\Pi}_m = \rho_m \vec{v} = \frac{\epsilon_r \mu_r - 1}{\mu_r} \frac{\vec{E} \times \vec{B}}{c^2} = - \frac{\vec{E} \times \vec{H}}{c^2}. \quad (\text{A1})$$

Consequently, the corresponding instantaneous mechanical force density

$$\vec{F}_m = \partial_t \vec{\Pi}_m = - \partial_t \left(\frac{\vec{E} \times \vec{H}}{c^2} \right) = - \partial_t \left(\frac{\vec{S}}{c^2} \right) \quad (\text{A2})$$

is opposite to the electromagnetic power flow represented by Poynting's vector \vec{S} . For the 3D dipole case, if one assumes that the current spectrum is $I(\omega) = I_0 F(\omega)$, the average power flow

$$\begin{aligned} \vec{S}_{ave}(\omega) &= \frac{1}{2} \left[- \frac{Z_{dipole}(\omega) I_0 \ell}{4\pi a^2} F(\omega) \hat{z} \sin \theta \right] \\ &\quad \times \left[\frac{I_0 \ell}{4\pi r^2} F^*(\omega) \hat{\phi} \sin \theta \right] \\ &= \left[\frac{1}{2} Z_{dipole}(\omega) |I(\omega)|^2 \right] \left(\frac{\ell}{4\pi a} \right)^2 \frac{1}{r^2} \hat{\rho} \sin^2 \theta. \end{aligned} \quad (\text{A3})$$

Consequently, the mechanical force density, Eq. (A2), in a matched zero-index medium is proportional to the power feeding the source, is inversely proportional to the square of the distance from the source, and is directed towards the source axis.

Note that although the underlying structure of the wave interactions treated here are transverse in character, an electromagnetic matched zero-index medium supports both transverse and longitudinal waves much like a cold plasma medium does. However, because the permittivity and permeability are both zero in the zero-index case, the dispersion relations for both types of waves are the same. Thus, the zero-index transverse waves behave similarly to their longitudinal counterparts, i.e., they behave like a collective mode (plasmon) of the zero-index medium.

It is intriguing, yet highly speculative, to consider the possibility that a graviton, a plasmon of the vacuum, might be a collective mode of a zero-index medium characterized by the gravitoelectric permittivity $\epsilon_g(\omega)$ and gravitomagnetic permeability $\mu_g(\omega)$ [26–28]. In particular, the time-harmonic form of the wave equation for the scalar potential associated with a point mass source M_g located at the origin in such a medium would be

$$\nabla^2 \Psi_g + \omega^2 \epsilon_g \mu_g \Psi_g = + 4\pi G M_g \delta(\vec{r}), \quad (\text{A4})$$

where G is the gravitational constant. The required Green's function or propagator is well known; the gravitational potential would thus have the form

$$\Psi_g(r, \theta, \phi; \omega) = -GM_g \frac{e^{-jk_g r}}{r}, \quad (\text{A5})$$

where $k_g = \omega \sqrt{\epsilon_g(\omega)} \sqrt{\mu_g(\omega)}$. If the index of the medium is zero near the frequency $f_0 = \omega_0/2\pi$, i.e., $\sqrt{\epsilon_g(\omega_0)} \sqrt{\mu_g(\omega_0)} = 0$, then the standard static gravitational potential is obtained:

$$\Psi_g(r, \theta, \phi; \omega_0) = -\frac{GM_g}{r}. \quad (\text{A6})$$

Because the equipotential surfaces are spherical in Eqs. (A5) and (A6), the corresponding force on a test mass m would be radial and would have an inverse-square distance dependence, i.e., $\vec{F}_g = -m\vec{\nabla}\Psi_g$. Thus, despite the underlying processes being wavelike, the fields would have a static spatial

behavior. It is noted that Whittaker made a different but related observation [29] that a sum of propagating spherical waves can also produce this static potential. While it is usually assumed that gravitational waves are propagating at the speed of light in vacuum [30–32], neither the zero-index results above nor those in [29] suggest that the speed of a gravitational wave would be $c = 1/\sqrt{\epsilon_0\mu_0} = 1/\sqrt{\epsilon_{g0}\mu_{g0}}$. In fact, as with the electromagnetic matched zero-index Drude medium result, one would suggest that the group speed of the gravitational waves could be different from c and its explicit value would depend on the specific dispersion models for $\epsilon_g(\omega)$ and $\mu_g(\omega)$. It would be interesting to reexamine several gravitational and vacuum polarization models to determine whether this type of zero-index description is indeed plausible.

-
- [1] A. Sanada, C. Caloz, and T. Itoh, *IEEE Microw. Wirel. Compon. Lett.* **19**, 68 (2004).
- [2] C. Caloz and T. Itoh, *Proceedings of the International Conference on Electromagnetics in Advanced Applications, ICEAA'03, Torino, Italy, 2003* (Politecnico di Torino, Torino, Italy, 2003).
- [3] C. Caloz, A. Sanada, and T. Itoh, *IEEE Trans. Microwave Theory Tech.* **52**, 980 (2004).
- [4] A. K. Iyer and G. V. Eleftheriades, in *IEEE MTT-S International Microwave Symposium Digest, Seattle, Washington, 2002* (IEEE, Piscataway, NJ, 2002), p. 1067.
- [5] G. V. Eleftheriades, A. K. Iyer, and P. C. Kremer, *IEEE Trans. Microwave Theory Tech.* **50**, 2702 (2002).
- [6] A. Grbic and G. V. Eleftheriades, in *IEEE International Symposium on Antennas and Propagation Digest, San Antonio, Texas, 2002* (IEEE, Piscataway, NJ, 2002), Vol. 4, p. 340.
- [7] A. Grbic and G. V. Eleftheriades, *J. Appl. Phys.* **92**, 5930 (2002).
- [8] R. W. Ziolkowski and C.-Y. Cheng, *Radio Sci.* **39**, RS2017 (2004).
- [9] S. Enoch, G. Tayeb, P. Sabouroux, N. Guérin, and P. Vincent, *Phys. Rev. Lett.* **89**, 213902 (2002).
- [10] S. Enoch, G. Tayeb, and D. Maystre, in *Electromagnetic Waves*, edited by J. A. Kong, Progress in Electromagnetics Research Vol. 41 (EMW, Cambridge, MA, 2003), pp. 61–81.
- [11] G. Tayeb, S. Enoch, P. Vincent, and P. Sabouroux, in *Proceedings of the International Conference on Electromagnetics in Advanced Applications, ICEAA'03* [2].
- [12] N. Garcia, E. V. Ponzovskaya, and J. Q. Xiao, *Appl. Phys. Lett.* **80**, 120 (2002).
- [13] B. T. Schwartz and R. Piestun, *J. Opt. Soc. Am. B* **20**, 2448 (2003).
- [14] R. W. Ziolkowski and E. Heyman, *Phys. Rev. E* **64**, 056625 (2001).
- [15] R. W. Ziolkowski, *Opt. Express* **11**, 662 (2003).
- [16] R. W. Ziolkowski and A. Kipple, *Phys. Rev. E* **68**, 026615 (2003).
- [17] D. G. Dudley, *Mathematical Foundations for Electromagnetic Theory* (IEEE, Piscataway, NJ, 1994), pp. 153–166.
- [18] J. Spanier and K. B. Oldham, *An Atlas of Functions* (Hemisphere, New York, 1987).
- [19] C. A. Balanis, *Antenna Theory*, 2nd ed. (Wiley, New York, 1997), pp. 133–136.
- [20] R. W. Ziolkowski, *IEEE Trans. Antennas Propag.* **51**, 1516 (2003).
- [21] L. Martín-Moreno, F. J. Garcia-Vidal, H. J. Lezac, A. Degiron, and T. W. Ebbesen, *Phys. Rev. Lett.* **90**, 167401 (2003).
- [22] P. Kramper, M. Agio, C. M. Soukoulis, A. Birner, F. Müller, R. B. Wehrspohn, U. Gösele, and V. Sandoghdar, *Phys. Rev. Lett.* **92**, 113903 (2004).
- [23] E. Moreno, F. J. Garcia-Vidal, and L. Martín-Moreno, *Phys. Rev. B* **69**, 121402(R) (2004).
- [24] J. P. Gordan, *Phys. Rev. A* **8**, 14 (1973).
- [25] A. Feigel, *Phys. Rev. Lett.* **92**, 020404 (2004).
- [26] V. B. Braginsky, C. M. Caves, and K. S. Thorne, *Phys. Rev. D* **15**, 2047 (1977).
- [27] B. Mashhoom, H. J. Paik, and C. M. Will, *Phys. Rev. D* **39**, 2825 (1989).
- [28] N. Li and D. G. Torr, *Phys. Rev. D* **43**, 457 (1991).
- [29] E. T. Whittaker, *Math. Ann.* **57**, 333 (1903).
- [30] R. L. Forward, *Proc. IRE* **49**, 892 (1961).
- [31] L. D. Landau and E. M. Lifshitz, *The Classical Theory of Fields*, 3rd ed. (Addison-Wesley, Reading, MA, 1971).
- [32] Richard P. Feynman, F. B. Moringo, and W. G. Wagner, in *Feynman Lectures on Gravitation*, edited by B. Hatfield (Addison-Wesley, Reading, MA, 1995), pp. 218–220.